Medical Image Analysis 13 (2009) 91–104

Contents lists available at ScienceDirect

Medical Image Analysis

journal homepage: www.elsevier.com/locate/media

# Modelling of image-catheter motion for 3-D IVUS

Misael Rosales [a], Petia Radeva [b], Oriol Rodriguez-Leor [c], Debora Gil [d,*]

[a] Laboratorio de Física Aplicada, Facultad de Ciencias, Departamento de Física, Universidad de Los Andes Mérida, Venezuela
[b] Centre de Visió per Computador, Universitat de Barcelona, Spain
[c] University Hospital "Germans Tries i Pujol", Badalona, Spain
[d] Centre de Visió per Computador, Universitat Autonoma de Barcelona, Spain

ARTICLE INFO

*Article history:*
Received 12 January 2007
Received in revised form 13 June 2008
Accepted 19 June 2008
Available online 3 July 2008

*Keywords:*
Intravascular ultrasound (IVUS)
Motion estimation
Motion decomposition
Fourier

ABSTRACT

Three-dimensional intravascular ultrasound (IVUS) allows to visualize and obtain volumetric measurements of coronary lesions through an exploration of the cross sections and longitudinal views of arteries. However, the visualization and subsequent morpho-geometric measurements in IVUS longitudinal cuts are subject to distortion caused by periodic image/vessel motion around the IVUS catheter. Usually, to overcome the image motion artifact ECG-gating and image-gated approaches are proposed, leading to slowing the pullback acquisition or disregarding part of IVUS data. In this paper, we argue that the image motion is due to 3-D vessel geometry as well as cardiac dynamics, and propose a dynamic model based on the tracking of an elliptical vessel approximation to recover the rigid transformation and align IVUS images without loosing any IVUS data. We report an extensive validation with synthetic simulated data and *in vivo* IVUS sequences of 30 patients achieving an average reduction of the image artifact of 97% in synthetic data and 79% in real-data. Our study shows that IVUS alignment improves longitudinal analysis of the IVUS data and is a necessary step towards accurate reconstruction and volumetric measurements of 3-D IVUS.



## 1. Introduction

The introduction of intravascular ultrasound (IVUS) in the field of medical imaging (Yock et al., 1988; Graham et al., 1989; Mintz et al., 2001; Wahle et al., 1999; Evans et al., 1996) as an exploratory technique has significantly changed the understanding of arterial diseases of coronary arteries. Each IVUS plane visualizes the cross-section (Fig. 1a) of the artery allowing, among others the assessment of different vessel plaques (thrombus of the arteriosclerotic plaques and calcium deposits) and the determination of morpho-geometric parameters (Metz et al., 1992, 1998; Jumbo and Raimund, 1998). 3-D IVUS is obtained by assembling in a stack 2-D IVUS images acquired during an automatic pullback of the catheter. 3-D IVUS is of great clinical interest as it allows to evaluate and quantify the effect of atherosclerotic plaque on arterial distensibility (Giannattasio et al., 2001), to follow-up the plaque and lumen after intervention (Nissen, 2002), and to guide the selection of an optimal interventional procedure (Nissen and Yock, 2001). Cardiac dynamics ( Mario et al., 1995; Delachartre et al., 1999; Roelandt et al., 1994; Thrush et al., 1997) and 3-D shape of the vessel (Wahle et al., 1999) introduce an image misalignment that can be appreciated in the IVUS sequence as a rotation and displacement of the vessel cross-section. This is a main artifact that hinders the longitudinal visualization of vessel morphology and any accurate assessment of morphological structures along the data sequence. Their effect in 3-D IVUS images has been described (Wahle et al., 1999; Nadkarni et al., 2005; Di Mario et al., 1993, 1995; Berry et al., 2000; de Korte, 1999; Bruining et al., 1998; Dijkstra et al., 1998) as a "saw-tooth-shaped" longitudinal appearance of the vessel wall that decreases precision in volumetric measurements. Intrinsic rotation and translation of the imaging catheter introduce artifacts in the longitudinal views making structures to appear and disappear as well as provoking tooth-shaped adventitia and calcified plaque, etc. This motion mainly affects the computation of the vessel diameter in the L-views. Fig. 1b shows the sinusoidal wavy pattern of the vessel wall due to the heart dynamics and blood pulsation that troubles the vessel wall detection and analysis of vessel structures along the sequence. The most disturbing phenomenon induced by vessel periodic motion is that the displacement invalidates any point correspondence along the sequence as, given a fixed angle in the short-axis IVUS image, points from different temporal frames do not correspond to the same vessel wall segment.

On the other hand, if we project the grey-level pixels in the temporal direction (longitudinal vessel direction) of the IVUS sequences, we can observe that salient features usually representing the calcium and fibrous plaque and adventitia-media borders describe a trajectory of semi-rotation of a ring around a stick (in this case, the catheter) (Fig. 1c). That is, in the short-axis

* Corresponding author.
*E-mail address:* debora@cvc.uab.es (D. Gil).

1361-8415/$ - see front matter © 2008 Elsevier B.V. All rights reserved.
doi:10.1016/j.media.2008.06.012

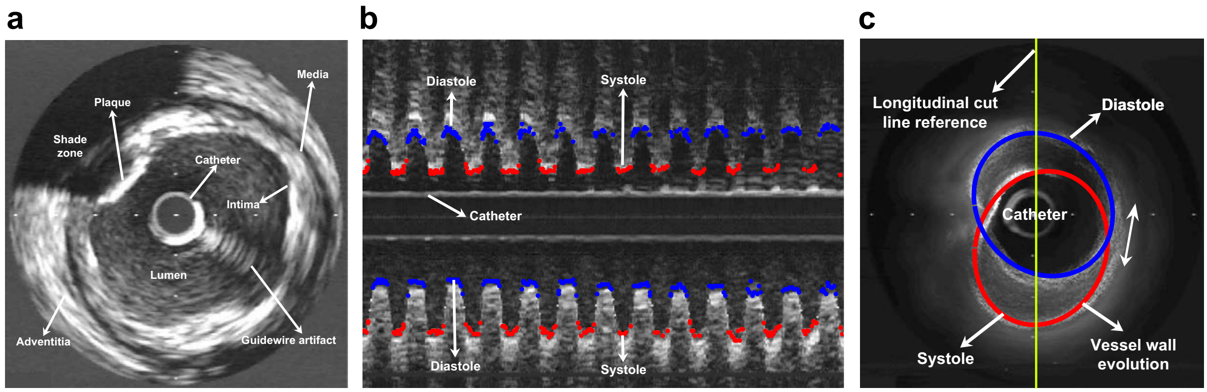


**Fig. 1.** Morphological arterial structures and artifacts in an IVUS image (a). Sinusoidal shape in a longitudinal cut (b) and grey-level shift in cross sectional view (c). Red and blue ellipses show the location of vessel wall at systole and diastole, respectively.

view, the rotation and translation of the catheter lead to high amount of vessel motion.

A usual strategy used to minimize the impact of the above described artifacts is to synchronize sequence acquisition with heart dynamics. This can be achieved by either special ECG-gated devices (Bruining et al., 1998) or by an image-based ECG-gated 3-D IVUS (De Winter et al., 2004; O'Malley et al., 2007, 2008). In the first case, a special ultrasonic device performing the catheter pullback at the same systolic peak is required and the acquisition time significantly increases. In the second case, one discards all frames between two consecutive systolic peaks, thus, running the risk of loosing valuable information. Keeping all frames and aligning them by suppressing their rotation and displacement would allow to get reliable radial measurements during the whole cycle related to the estimation of the elastic properties of the vessel. Alternatively, reconstructing the path using biplane angiography (Evans et al., 1996; Wahle et al., 1999) could alleviate the geometric distortions due to the position and angular rotation of the catheter by tracking the Frenet triangle according to the vessel tortuosity, although in this case, image rotation due to heart dynamics is not considered.

The goal of this work is to estimate and remove the rigid motion effect by using only IVUS images keeping at the same time all the data. The complex movement of the imaging catheter inside the coronary vessel causes motion artifacts that can be explained by three phenomena: (a) rotation of the IVUS imaging catheter with respect to the vessel (i.e. around the axis tangential to the catheter), (b) translation of the imaging catheter in the plane perpendicular to the catheter axes, and (c) translation of the catheter along its axis forward and backward causing a swinging effect. In this paper, we address the first two motion artifacts in order to help the short-axis as long-axis vessel display, to visualize and quantify different morphological vascular structures like plaque, stents, lumen diameter, lesions, etc.

We present a hypothesis that the vessel wall motion in IVUS images is due to two main factors: a systematic contribution caused by vessel wall geometry and a dynamical periodic contribution due to the heart pulsatile contraction influence. This decomposition of the vessel profiles serves to model the vessel dynamics and determines a robust procedure for vessel motion suppression. Aiming to correct rigid transformation the vessel wall is approximated by an elliptical model that is tracked in IVUS frames to estimate its rotation and translation. The elliptical approximation (Andrew et al., 1999) is computed on a rough segmentation of salient vessel structures using a Neural Network algorithm (Patrick, 1994). By applying our stabilization approach, vessel appearance in short-axes views allows better and easier perception of vessel structures distribution and quantity. In longitudinal views we remove the tooth-shape and thus assure that changes in vessel diameter are due to changes in morphology. In this way, we ease the analysis of plaque progression along the vessel compared to the original L-views. Note that this step is crucial for a further analysis of vessel biomechanics (palpography, measuring elastic properties as strain or stress, etc.) since their computation requires tracking material points of the vessel along the cardiac cycle.

Recently there has been an increasing interest in compensating motion (Danilouchkine et al., 2006; Leung et al., 2006, 2005) of the whole stack of IVUS images in order to improve tissue elastographic studies. The existing approaches for motion compensation in IVUS rely on either registration (Leung et al., 2006) or tracking (Danilouchkine et al., 2006) of image intensities. In Leung et al. (2005) the authors report several techniques as follows: (1) Global rotation block matching (GRBM), (2) contour mapping (CMAP), (3) local block matching (LBM) and (4) catheter rotation and translation (CRT). These methods are based on similarity estimation of local image features defining a ROI on frames of interest. However, when the IVUS segment sequence does not possess any characterizing structure, the similarity between blocks can become very sensitive. In the GRBM case, the minimizing algorithm is prone to get stuck at a local minima unless exhaustive (computationally inefficient) search is performed. In the case of tracking algorithms, large displacements cannot be properly modelled. In any case, changes in image intensity from one frame to the next one substantially affect the performance of the algorithms.

Our method is based on registering the global representation of vascular structures defined by the geometry of the coronary vessel. The proposed approach does not require any minimization process, since parameters are given by an explicit formula. It follows that our computation of motion parameters is not affected by any intensity changes between consecutive frames. Furthermore, since points on vessel structures are computed separately on each image, our methodology naturally handles large displacements. An advantage of our strategy is that it does not need a very precise segmentation of vessel structures in order to correct vessel motion. The set of reported experiments includes vessel motion simulations and validation of vessel dynamics suppression in real-data of 30 patients. Our results reveal suppression of rigid transformation up to 97% in synthetic data and up to 85% in real-data.

The paper is organized as follows: The theoretical grounds of the model are given in Section 2: assumptions on vessel dynamics are presented in Section 2.1 and the mathematical formulation in Section 2.2. Our approach to computation of parameters is given in Section 3. Experiments are reported in Section 4 validating the model on phantom data in Section 4.1 and results on experimental data in Section 4.3. The article finishes with Discussions and Conclusions.

## 2. A dynamical model of vessel wall appearance in IVUS

### 2.1. Model assumptions

The dynamics of a coronary artery is mainly governed by the left ventricle dynamic evolution, blood pressure and intrinsic geometric vessel properties (Mazumdar, 1992; Young and Heath, 2000; Nadkarni et al., 2003; Holzapfel et al., 2002). The first order approximation to vessel dynamics is given by a linear transformation combining translation, rotation and scaling (Waks et al., 1996). The main assumptions in the model we propose are the following:

1. Vessel translation and rotation have two main contributions: a dynamic periodic motion and a systematic geometric one.
   Vessel displacement along the sequence is reflected by the vessel wall profile in longitudinal cuts (Gil et al., 1996). Visual inspection of large longitudinal cuts (see Fig. 2) shows that there is a periodic wavy profile (blue and red sinusoidal lines) and a systematic contribution (green base-line).
   We take the temporal evolution of the lumen center along the sequence as the main descriptor of vessel displacement. The lumen centers were estimated as the centers of an elliptical approximation to the vessel wall points. The spatial variation of the lumen center, $(\Delta x, \Delta y)$, is a main geometric measure that provides with relevant information on heart dynamics and geometric contributions to the IVUS displacement. Fig. 3a shows the spatial evolution of the lumen center horizontal coordinate, $\Delta x$. We note that such profile decomposes into two main curves: a cardiac periodic oscillation (blue line) and a base curve (red thick line) representing vessel wall position. The power spectral density (Fig. 3b) reflects these two main phenomena, as there are two predominant frequency ranges.
   Low frequencies (in the range $(b1,b2) = (0.02, 0.33)$ Hz) correspond to the geometric lumen evolution, while, those frequencies located at $(b3,b4) = (0.78,\ 0.91)$ Hz are heart dynamics contributions. By the above considerations, we decompose lumen displacement into geometric, $(\Delta x_g, \Delta y_g)$, and dynamical, $(\Delta x_d, \Delta y_d)$, contribution terms: $\Delta x_g + \Delta x_d$ and $\Delta y = \Delta y_g + \Delta y_d$. The decoupled terms are given by the Fourier series:

$$\Delta x_g(t) = \sum_{n=b_1}^{n=b_2} (A_n \cos(n\omega t) + B_n \sin(n\omega t)),$$
$$\Delta y_g(t) \sum_{n=b_1}^{n=b_2} (A_n \cos(n\omega t) + B_n \sin(n\omega t)) \quad (1)$$

$$\Delta x_d(t) = \sum_{n=b_3}^{n=b_4} (C_n \cos(n\omega t) + D_n \sin(n\omega t)),$$
$$\Delta y_d(t) \sum_{n=b_3}^{n=b_4} (C_n \cos(n\omega t) + D_n \sin(n\omega t)) \quad (2)$$

   Using similar argumentations, we also decouple the angle of rotation, $\Delta\alpha$, into geometric and dynamical terms:

$$\Delta\alpha_g(t) \sum_{n=b_1}^{n=b_2} (A_n^\alpha \cos(n\omega t) + B_n^\alpha \sin(n\omega t)),$$
$$\Delta\alpha_d(t) \sum_{n=b_3}^{n=b_4} (C_n^\alpha \cos(n\omega t) + D_n^\alpha \sin(n\omega t))$$

   These Fourier coefficients give the heart dynamics and geometric contributions amplitudes to vessel motion and play a central role in the simulation of vessel dynamic profiles (see experimental Section 4).
2. Wall shape evolution can be described by means of the rotation and translation of an elliptical model.
   In order to correct rigid motion artifacts due to the relative displacement of the vessel versus the imaging catheter, we restrict the vessel wall evolution to a rigid transformation, that is, a translation followed by a rotation. There are two possible ways of computing such transformations: registration of IVUS data based on image gray level (Lester and Arridge, 1999) or correspondence of vessel structures/vessel border (Rosales et al., 2005).
   Using an intensity based image registration runs the risks of aligning images taking into account the most external part of the image, which contain no structural information on vessel borders but are mainly shadow and bright artifact areas. In order to avoid such misalignment, we track the most salient vessel structures located around the interface intima, media and adventitia. To such purpose, points conforming to the gray value characteristics defining the transition lumen-tissue are extracted by means of a neural network vessel wall detection (see Section 3). Instead of searching for points correspondence between two consecutive frames, for the sake of a robust and efficient approach, we extract and track a global model of the set of points extracted. Since we focus on a global linear rigid transformation an elliptic model suits our purposes. The motion-tracking algorithm will succeed as far as the computed elliptic model keeps stable along the sequence since, in this case, any artifact due to an unsuccessful fitting does not affect the elliptical vessel wall approximation.

### 2.2. Model formulation

The above assumptions on vessel dynamics and the elliptical shape approximation of vessel cross sections simplify the formulation of vessel motion to describing a rigid transformation of an elliptical vessel wall shape.

The vessel wall $\gamma_k(u) = (x_k(u), y_k(u))$ at time $t_k$ can be written as follows:

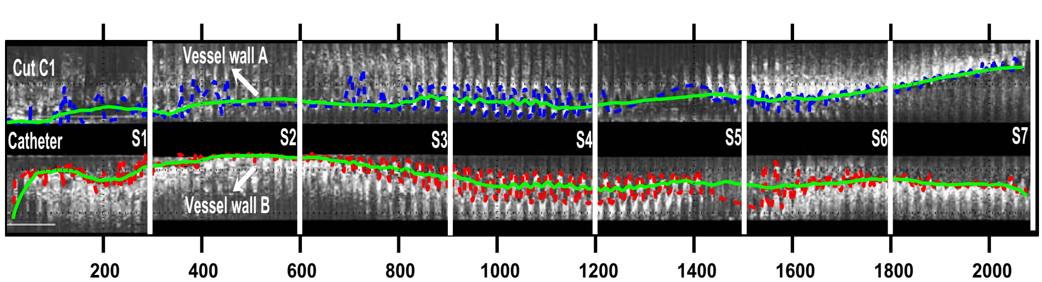


**Fig. 2.** Longitudinal cut of IVUS data acquired during the catheter pullback. Blue and red points show the upper and down vessel wall boundary. The green line shows the systematic contribution of catheter motion.

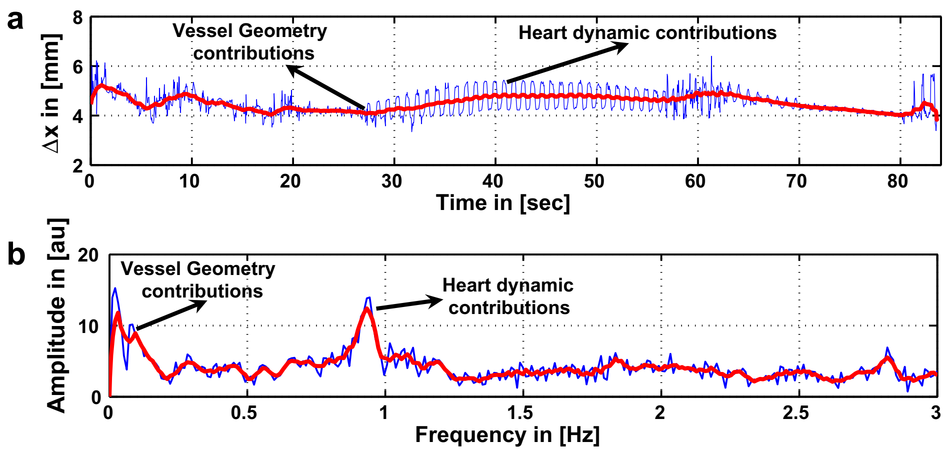


**Fig. 3.** Temporal evolution of the lumen center $\Delta x$ coordinate (a) and its Fourier spectrum (b). Red lines show vessel geometry contribution and blue line illustrates the heart dynamic contribution.

$$x_k(u) = a * \cos(\theta(u) + \delta_k) + cx_k$$
$$y_k(u) = b * \sin(\theta(u) + \delta_k) + cy_k \tag{3}$$

where $0 < \theta \leqslant 2\pi$ determines the angular position of the corresponding point on the ellipse, $u$ is the internal parameter of the model curve, $(a,b)$ are the minor and major radii of the ellipse, $\delta_k$ is its orientation and $C_k = (cx_k, cy_k)$ is its center. We assume that the lumen center $C_k$ of $\gamma_k$ can be changed from position $(cx_k, cy_k)$ at time $t_k$ to $C_{k+1}$ with position $(cx_{k+1}, cy_{k+1})$ at time $t_{k+1}$ due to the periodic heart movement. Therefore, the position of the center $C_{k+1}$ of the new vessel shape $\gamma_{k+1}$ at time $t_{k+1}$ can be written as

$$cx(t_{k+1}) = cx(t_k) + \Delta x_k, cy(t_{k+1}) = cy(t_k) + \Delta y_k \tag{4}$$

where $\Delta x$ and $\Delta y$ give the geometric and dynamical change induced by the vessel geometry and heart pulsatile contribution on the lumen center spatial and temporal evolution, given by Eqs. (1) and (2).

When changing to the new lumen center, a new rotated vessel wall $\gamma_{k+1} = (x_{k+1}, y_{k+1})$ is given, which coordinates have changed according to a rotation of angle $\alpha_k$. Using the image center as rotational center, the new vessel wall coordinates can be written as

$$\begin{pmatrix} x_{k+1}(u) \\ y_{k+1}(u) \end{pmatrix} = \begin{pmatrix} \cos(\alpha_{k+1}) & \sin(\alpha_{k+1}) \\ -\sin(\alpha_{k+1}) & \cos(\alpha_{k+1}) \end{pmatrix} \begin{pmatrix} x_k(u) \\ y_k(u) \end{pmatrix} \tag{5}$$

Thus, if we know the rotation angle $\alpha_k$ at each time $k$, we are able to find the corresponding material point position in the next frame. In order to obtain the rotation angle we define as a reference point, the point of the vessel model closest to the rotation center approximated by the center of the image. The angle determined by the vectors of the reference point in each pair of consecutive images determine the rotation angle for these frames. Fig. 4a shows the relation of geometric parameters of our model. Without loss of generality, to illustrate our approach we use a circular vessel model. Fig. 4a is showing two vessel models $\gamma_1$ and $\gamma_2$ with their corresponding centers $C_1$ and $C_2$ and rotation angle $\Delta\alpha$. Note that $\alpha_{k+1}$ can be written as $\alpha_{k+1} = \alpha_k + \Delta\alpha_k$, where $\alpha_{k+1} = \arctan(cy_k/cx_k)$ and

$$\Delta\alpha_k = \arctan((cy_k + \Delta y_k)/(cx_k + \Delta x_k)). \tag{6}$$

## 3. A procedure for rigid motion estimation and suppression

The procedure for rotation suppression splits into three main steps:

- *Elliptical vessel approximation* – this step consists in vessel detection by a Neural Network trained to classify salient structures of vessel border and elliptical approximation of the vessel wall.
- *Motion parameters computation* – this step consists in estimation of the rotation along the image sequence using tracking procedure of a reference point.
- *Image motion correction* – this step consists in correction of image rotation and displacement using the extracted parameters of the elliptical approximation.

### 3.1. Elliptical vessel approximation

For the computation of the vessel elliptical representation, structures on vessel wall along the sequence must be located. The detection of the vessel wall is based on physical parameters that characterize the intima, media and adventitia layers. Such descriptors are defined by global and local image grey-level properties obtained from IVUS images in polar form (Rosales et al., 2004) with the origin at the catheter center. In this coordinate system, the image intensity, namely $I$, depends on the pixel distance (radius $r$ in polar coordinates) to the ultrasound transducer (Jensen, 2001; Vogt et al., 1998). The decrease in the initial beam intensity, $I_0$, is exponentially proportional to the absorption coefficient $\zeta$, the frequency of the ultrasound, $f$, and the particle size or scatterer number, $N_\theta$, located along the ultrasound beam path:

$$I(r) = I_0 \exp(-\zeta N_\theta f r).$$

The absorption coefficient gives the rate of diminution with respect to the distance along a transmission path (Jensen, 2001) and it is locally obtained from the regression line slope (Vogt et al., 1998) of the image profile. Fig. 5a shows a radial grey-level profile of an IVUS image, the lumen-vessel border is approximately represented by the steepest grey-level transition that is used to train the Neural Network.

The set of characteristics chosen to find salient points on the vessel wall are the absorption coefficient $\zeta$, image pixel grey-level $I(r)$ and radial standard mean $\mu$ and deviation $\sigma$ of the data. The absorption coefficient gives local information about the lumen-vessel transition acting as an edge detector. The statistics considered ($\mu$ and $\sigma$) contain regional information on vessel structures: $\mu$ gives the baseline of global grey-level intensity and $\sigma$ gives a simple descriptor of the regional texture. In order to find potential candidate structures on the vessel wall, a Perceptron Multilayer Neural Network (60:50:60:30) was trained using a standard Back

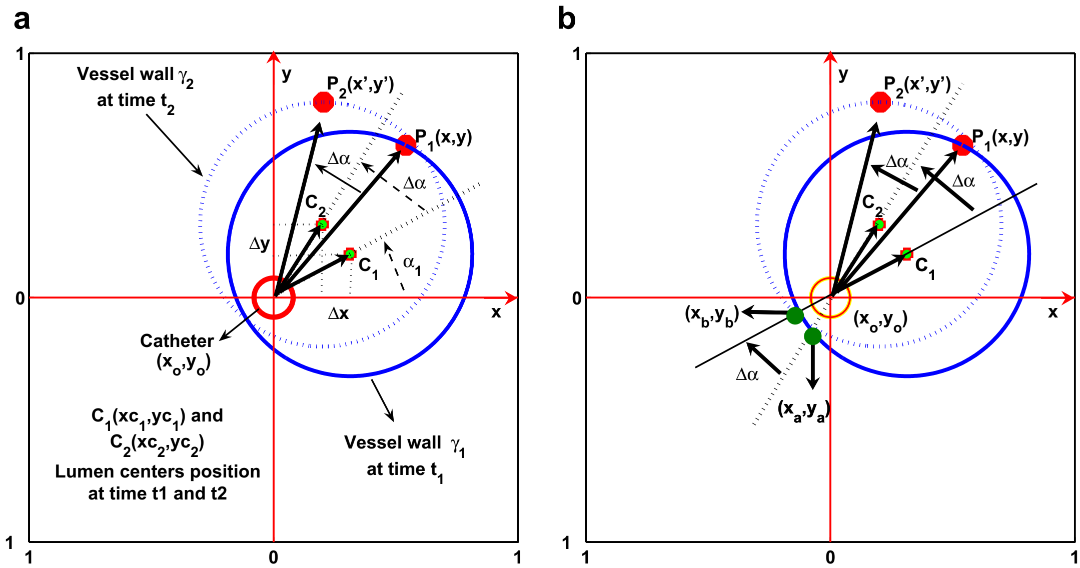


**Fig. 4.** Geometric parameters of the model (a). Estimation of the rotation angle $\alpha$ (b).

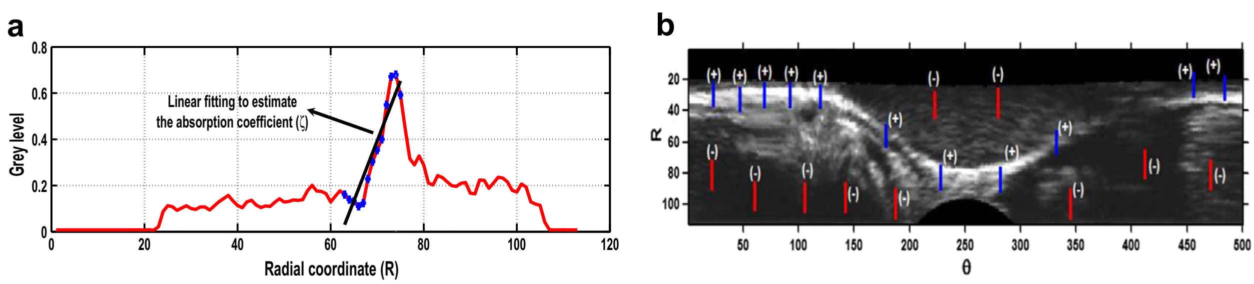


**Fig. 5.** Vessel structures location. Radial grey-level profile (a) and extraction of positive (+) and negative (−) patterns (b) to train the neuronal network.

Propagation Algorithm (Patrick, 1994). Fig. 5b shows training examples of a positive (+) corresponding to intima and negative (−) pattern, corresponding to blood, adventitia, shadows, and artifact zones. Once applied the neuronal network to classify salient points on the vessel border, an elliptical approximation to the vessel wall points is adjusted using the mean square ellipse fitting method described in Andrew et al. (1999).

### 3.2. Motion parameters computation

Once defined the ellipse center as new origin, it is necessary to estimate the angular rotation profile of the vessel wall structure. In a rotation, it is sufficient to provide the temporal evolution of a single point on the vessel wall structure (Kittel et al., 1991; Broucke, 1978), to measure the angular difference between two consecutive frames. Since the ultrasound intensity gradually decreases in the radial direction, it follows that one of the best visible structure points on the vessel wall is the point nearest to the image center (Courtney et al., 2002; Rosales et al., 2004). The spatial location of this reference point is determined as the positions $(x_k^a, y_k^a)$ in frame $k$ and $(x_{k+1}^a, y_{k+1}^a)$ in frame $k+1$ on the vessel structure (see Fig. 4b) that have the minimal Euclidean distance to the image centers $(cx_k, cy_k)$ and $(cx_{k+1}, cy_{k+1})$. The distance criterion can be written as

$$(x_k^a, y_k^a) = \mathrm{argmin}_u((x_o - x_k(u))^2 + (y_o - y_k(u))^2)^{1/2}$$

where $x_k(u)$ and $y_k(u)$ are the coordinates of the points of the elliptical vessel model. written as

$$\alpha(t_k) = \alpha_0 + \Delta\alpha_k \tag{7}$$

where $\alpha_0 = \arctan(y_0^a/x_0^a)$ is the reference angle corresponding to the initial frame, and $\Delta\alpha_k \arctan(y_k^a/x_k^a)$ is the rotation angle of frame $k$.

### 3.3. Image motion correction

The suppression of the rotation is given by the following linear transformation. The current image frame $I_k(x,y)$ is translated by $(cx_k, cy_k)$ to center the ellipse on the image center, following by a rotation through an angle $-\alpha_k$:

$$\begin{pmatrix} x'_k \\ y'_k \end{pmatrix} = \begin{pmatrix} \cos(-\alpha_k) & \sin(-\alpha_k) \\ -\sin(-\alpha_k) & \cos(-\alpha_k) \end{pmatrix} \left( \begin{pmatrix} x_k \\ y_k \end{pmatrix} - \begin{pmatrix} cx_k \\ cy_k \end{pmatrix} \right) \tag{8}$$

where $(x'_k, y'_k)$ and $(x,y)$ are the new and old cartesian image coordinates, $\alpha_k$ is the rotation angle and $(cx_k, cy_k)$ is the elliptical center. By iteratively applying this equation, we achieve to align all frames within the IVUS sequence.

## 4. Validation and results

As mentioned above, our work is to use the geometric model to explain and remove the discontinuous longitudinal vessel appearance in IVUS data; hence, we plan the following set of experiments to validate the motion compensation procedure:

1. Robustness of the estimation of motion parameters – we check the impact of inaccuracies in the estimating of the ellipsoidal shape as well as the robustness of the estimation of motion parameters by means of a dynamic vessel phantom.
2. A robust measure of rotation suppression in experimental data – since in real cases it is difficult to know in advance the expected motion parameters, it is required to define first a quantity properly assessing the accuracy in motion correction. The synthetic phantom helps us to define a robust measure of rotation suppression in terms of the vessel wall profile in longitudinal cuts.
3. Assessment of motion suppression in real sequences – we check the efficiency of the proposed technique by a study of short sequences of 300 images each one extracted from 30 patients.
4. Stabilized Vessel Model – in order to illustrate the improvements provided by IVUS image alignment we show the results of a vessel reconstruction before and after correction.

### 4.1. Robustness of the estimation of motion parameters

The vessel phantom for motion correction is generated by applying a motion profile to synthetic IVUS images. The Fourier decomposition given in Section 2.1 serves to compute the rotation (Eqs. (6) and (7)) and the vessel displacement (Eqs. (1) and (2)) profiles. The result of adding heart dynamics contributions to vessel geometry is the sinusoidal blue line and the resulting geometric profile due to the catheter pullback in a tortuous vessel displayed by the red solid line in Fig. 6. We generated the vessel position corresponding to the different temporal frames and obtained the vessel profiles in the simulated longitudinal IVUS cuts. Two different phantom models have been used: an elliptical shape and a vessel profile extracted from real-data. The elliptical model allows to detect artifacts in the geometric computation of the rotation angle. The vessel shapes extracted from manual segmentation of IVUS sequences, assess the robustness of the method against the elliptic modelling of vessel borders. For the elliptical model we used 73 ellipses with eccentricities uniformly sampled in the range $[0,1]$. For the generation of the real-data based phantom, we used, for each frame $k$ only 25% of the vessel wall data points randomly selected. In this way we can check the model robustness to lack of information in diseased sections of the vessel.

The error measure used to assess the accuracy of the estimated rotation profiles is the absolute difference between angles computed from the true synthetic profile. The correlation coefficients (the slope, $m$, and the independent term, $b$) between the estimated angle and the theoretic one have been computed. In the ideal case of a perfect correlation $m = 1$ and $b = 0$. Fig. 7a shows the regression line obtained for an ellipse eccentricity with $\xi = 37.5\%$, with a slope $m = 1.03$ and $b = 0.23$. Fig. 7b shows the angular error as a function of the eccentricity $\xi$. When the catheter is near to the lumen center $(-10 \leqslant \xi \leqslant 10)$ the linear coefficient $m$ has a singularity due to the equidistance between the catheter center and the vessel wall points. In these cases, the reference point as the closest point to the catheter center, used to estimate the rotation angle makes no sense. In the case of real-data based phantoms (see Fig. 8), the linear coefficients present a stable behavior along the sequence, with statistical values for $m$ equal to $\mu \approx 1.02$, $\sigma \approx 0.1$. This represents approximately a 10% of error in the estimation of the rotation angle which, taking into account that only 25% of the vessel wall data point has been used, is an acceptable experimental result. The linear coefficient $b$ gives the base line angle between theoretical and experimental angle. The statistical values of $b$ were $\mu \approx 5$, $\sigma \approx 4$), hence, there is an acceptable base line shift between theoretic and real angle.

The advantages of incorporating vessel geometric information to the computation of its rigid dynamics are reflected in the accuracy achieved in synthetic phantoms. According to (Danilouchkine et al., 2006) only motion below 3.5° can be successfully modelled. For those rotations the mean absolute angular errors did not exceed 7.8°. Our methodology supports large rotations in the range $[-25, 25]$ degrees with an absolute error of $5 \pm 4°$. Errors statistical ranges between theoretic and estimated parameters where extracted from the regression coefficients (the slope $m$ and the independent term $b$) of the errors obtained for each vessel dynamic phantom. Since the average slope is 1.02, the range for the independent term reflects the range for the absolute error. Figs. 7 and 8 show the regression lines for an elliptic (Fig. 7a) and a real vessel profile (Fig. 8b) phantom models.

### 4.2. A robust measure of rotation suppression

Numerically checking to what extend the vessel wall rigid motion has been correctly computed can only be done in synthetic models, where the true displacement parameters are known. In the case of real images extraction of a quantitative measurement it is not possible and one has to base on motion correction in vessel wall visual appearance. Vessel profiles in longitudinal cuts and alignment of vessel salient structures are good candidates.

After a proper translation and rotation suppression (Pluim et al., 2003), the vessel shape appearance of a longitudinal cut is a straight line, as both saw-like periodic patterns and vessel curvature due to an origin different from lumen center have been removed (Seemantini et al., 2005; De Winter et al., 2004). We propose using the Euclidean distance, $\Delta d$, between the vessel profile and its linear fitting as objective measure of the amount of motion removed. Fig. 9 illustrates the mechanism followed to compute $\Delta d$ and the difference between the dynamic synthetic profile (Fig. 9a) and its corrected counterpart (Fig. 9b).

The statistical range (given by the mean ± standard deviation) of $\Delta d$ along the segment measures the reduction in vessel movement. The mean value of $\Delta d$ reflects the overall performance of the proposed suppression and the standard deviation measures its robustness. Fig. 10 displays $\Delta d$ histogram before (Fig. 10a) and after (Fig. 10b) rotation suppression for the real-data based

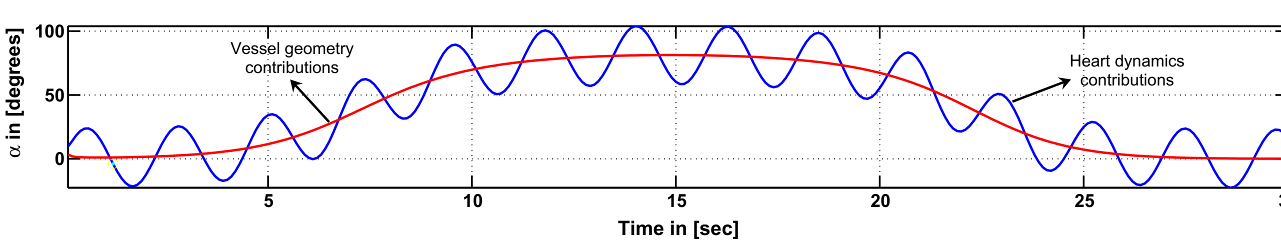


**Fig. 6.** Rotation profile for synthetic simulation of vessel dynamics. Blue line shows the heart dynamics contribution and the red line – the vessel geometry contribution.

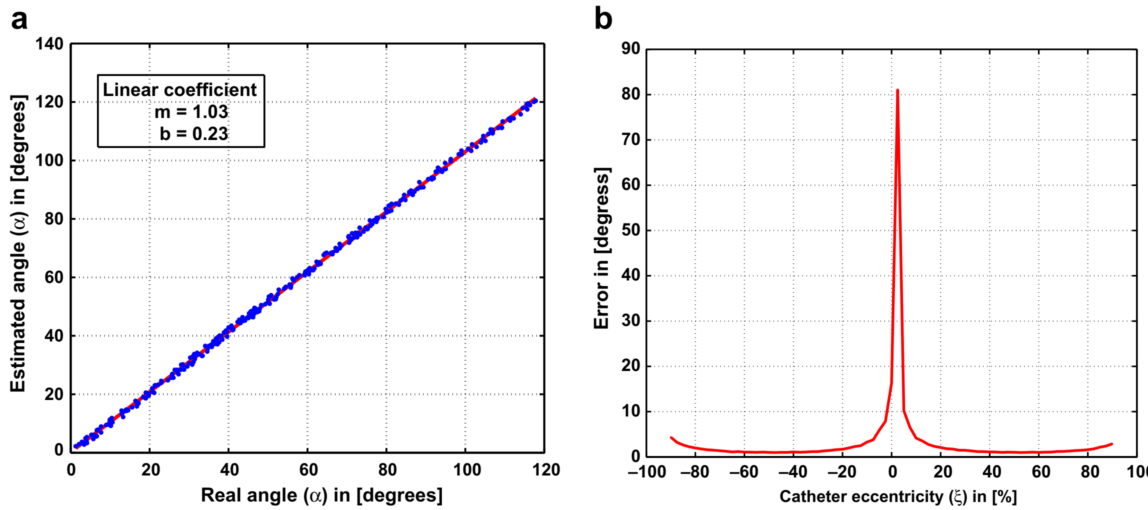


**Fig. 7.** Rotation estimation for elliptic phantom. Theoretical vs. estimated rotation profile for an eccentricity $\xi = 37.5\%$, (a), and error in angle estimation as a function of the ellipse eccentricity, (b).

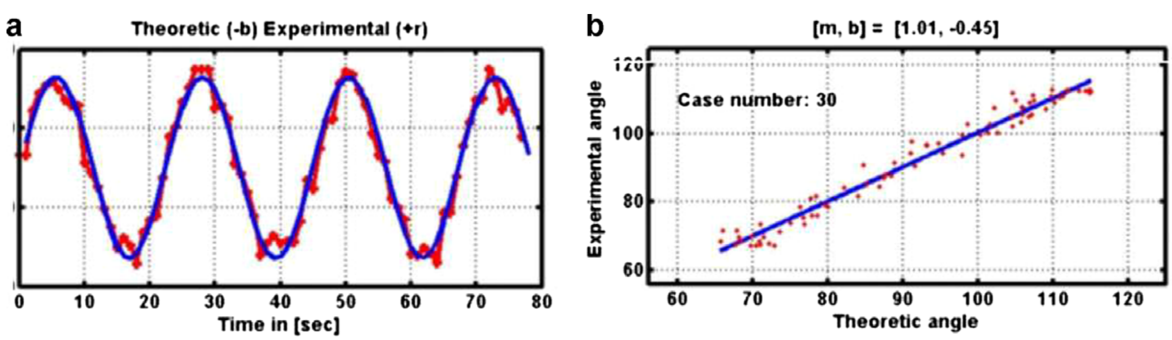


**Fig. 8.** Rotation estimation for real-data phantoms. Real (in blue) and estimated (in red) rotation profile (a) induced to a real vessel wall points and its linear correlation (b).

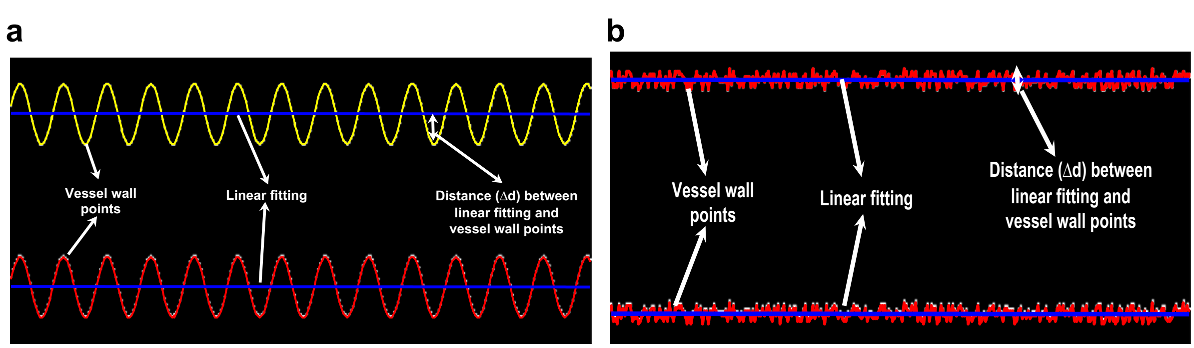


**Fig. 9.** Longitudinal cut before (a) and after (b) rotation suppression.

phantom. Before movement suppression, the distance distribution, $\Delta d_A$, is in the range $(1.1 \pm 0.5)$ mm, while after correction the distance, $\Delta d_B$, is within $(0.04 \pm 0.1)$ mm. This represents an average movement reduction of 97% and a straighten of the sinusoidal vessel wall shape induced by rotation and translation.

The ratio, $R$, between the distance after, $\Delta d_A$, and before, $\Delta d_B$, indicates the amount of movement suppressed. A value of zero is achieved when the vessel profile is a straight line and a value above 1 suggests that the algorithm has fails to reduce motion. In experimental data, radial dilation and vessel curvature prevent the ratio $R$ achieving its optimal lower bound even if rigid motion has been properly removed. In fact, in short segments, radial dilation is the main source of deviation from a straight pattern. According to clinical studies (Williams et al., 1999; Dodge et al., 1992) blood pressure introduces an average dilation of 14% of the vessel diameter. In order to take into account this baseline elastic deformation, we define a rigid ratio as

$$Rr = \frac{|\Delta d_A - 0.14 * \mathrm{VesselDiam}|}{\Delta d_B} \quad (9)$$

for VesselDiam the mean diameter of the vessel segment under study.

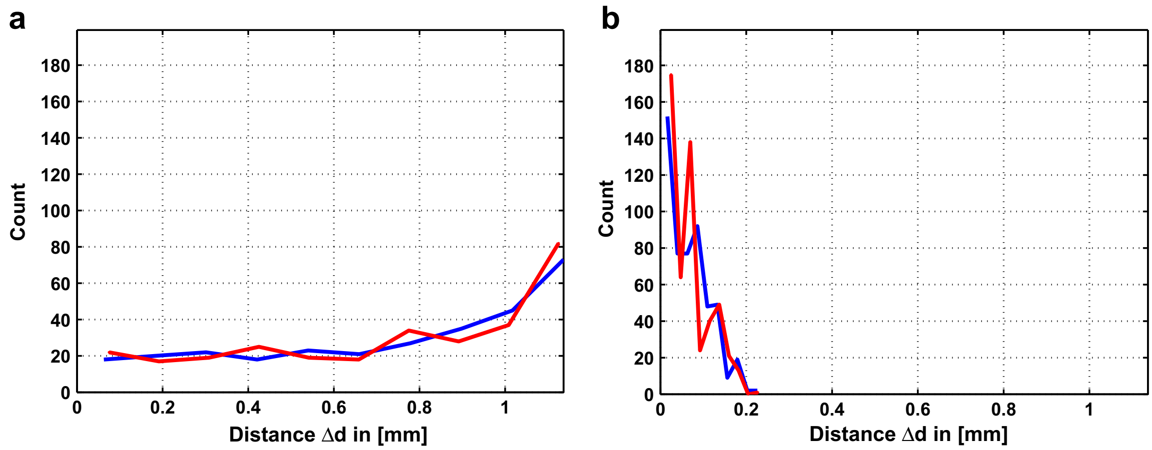


**Fig. 10.** Histogram of $\Delta d$ before (a) and after (b) rotation suppression.

### 4.3. Assessment of motion suppression in real sequences

In order to study the behavior of the reported motion suppression strategy we analyzed a set of sequences of 300 images each one for 30 patients independent from the set used to train the Neural Network. The sequences were acquired using a Boston Sci. equipment Boston Scientific Corporation, 1998 at 40 MHz at constant pullback speed of 0.5 mm/sec. The processing time can be divided in four steps (see Section 3):

1. *Neuronal network training* is relatively fast, since the main characteristics difference between vessel wall and the rest is notably large, nearly 5 min (using a PC Pentium at 2.4 GHz).
2. *Vessel wall detection* by Neuronal Network (0.08 s/image)
3. *Vessel wall elliptical fitting* (0.01 s/image).
4. *Correction of image rotation* and displacement using the extracted parameters of the elliptical approximation (0.01 s/image).

Longitudinal cuts before and after rotation elimination are shown in Fig. 11. One can notice the smoothing effect of the rotation correcting on the appearance of the lumen border (red line in Fig. 11) in the longitudinal view. Still complete smooth appearance of the vessel in the longitudinal images is not expected due to the different degree of radial expansion/contraction of the vessel (Fig. 11d and f) according to its elastic properties (since we remove/correct only rigid vessel motion effects). We should also take into account that by aligning vessel lumens, we have an optical artifact due to the external adventitia bright tissue and the catheter which adopt a wavy saw-shape appearance (see Fig. 11). The structures in longitudinal views that reflect correct alignment of vessel IVUS planes, are the ones bordered by the red lines that show the transition between blood and tissue. Correction of center position straightens the vessel profile (see Fig. 11b–c), removing most of the saw-shape effect if present (see Fig. 11d–f). Rotation correction produces an alignment of structures which is better appreciated in the presence of salient plaque such as calcium (bottom of Fig. 11a). The periodic vessel rotation produces shadow-bright banded profile at calcium sectors which disappears converting it into a uniform bright or dark band (as it is the case of Fig. 11a) meanwhile the rotation is suppressed. As for the geometric systematic rotation induced by the vessel geometry, it results in a continuous variation of salient structures which do not suddenly disappear but smoothly change along the longitudinal cut (see Fig. 11e).

Our statistical analysis focused on checking the robustness in parameter estimation as well as reduction in movement. Robustness in the estimation procedure is assessed by computing parameters of original and corrected images. Intuitively, we can assume that the less variation in parameters extracted from automatically computed still images, the more reliable the reported geometric motion estimation is. The standard deviation, $\sigma$, along each sequence indicates such variability for each parameter. The standard deviation in the radial position of the lumen centers before transformation correction presents a significative decrement for all cases from $\Delta r \approx (2.3 \pm 3)$ mm to $\Delta r \approx (0.5 \pm 0.3)$ mm after image alignment. In the case of rotation estimation, we have a reduction from $\delta\alpha \approx (69 \pm 20)^\circ$ before to $\delta\alpha \approx (11 \pm 8)$ degrees after rotation suppression that supposes 85% of rotation suppression. Fig. 12 shows the standard deviation of motion parameters for the 30 patients analyzed, lumen center position in Fig. 12a and rotation angle in Fig. 12b.

The quantitative assessment of motion reduction is given by the rigid ratio $Rr$ defined by (9) and using that the average vessel diameter in our data is approximately 2.5 mm. Fig. 13 shows the rigid ratio $Rr$ and its histogram in percentages (Fig. 13b) for the 30 cases. The range for $Rr$ in percentages is 79.30 ± 19.83 and in 76% of the cases is over 72%.

### 4.4. Stabilized vessel model

In order to obtain a realistic model of the vessel shape, we must separate the geometric vessel properties from heart dynamics contributions. Let $\gamma(t) = (x(t), y(t), z(t))$ be the vessel border as a function of time $t$ written as an elliptical approximation:

$$x(t) = a(t)\cos(\theta + \delta(t)) + cx(t),$$
$$y(t) = b(t)\sin(\theta + \delta(t)) + cy(t), \quad z(t) = cz(t) \qquad (10)$$

where $(0 < \theta \leqslant 2\pi)$, $(a(t), b(t))$ are the minor and major radii of the ellipse, $\delta(t)$ is its orientation and $C = (cx(t), cy(t), cz(t))$ its center. In 2.5-D IVUS reconstruction $cz(t)$ is unknown, but in our model we can take it as the catheter position in longitudinal direction, $cz = vt$, where $v$ is the catheter velocity. Taking into account the decoupling into geometrical and heart dynamics contributions given in Section 2.1, the vessel wall parameters can be written as

$$a(t) = a_g(t) + a_d(t), \quad b(t) = b_g(t) + b_d(t)\delta(t) = \delta_g(t) + \delta_d(t)$$
$$cx(t) = cx_g(t) + cx_d(t), \quad cy(t) = cy_g(t) + cy_d(t)$$

where the subscript $g$ stands for the geometric component and the $d$ for the periodic heart movement. In order to reconstruct the vessel wall from catheter point of view only the Fourier coefficient that corresponds to geometrical contribution must be taken into account, so that Eq. (10) reduces to

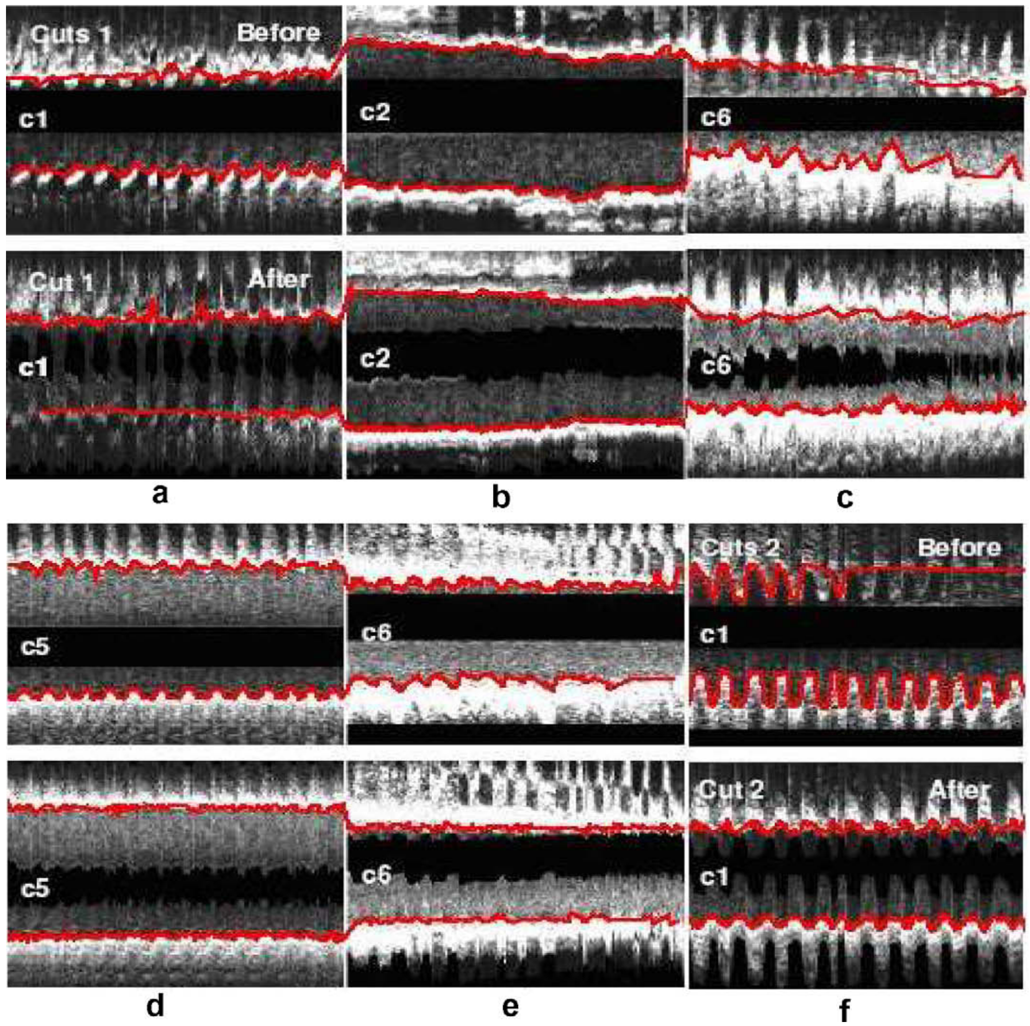


**Fig. 11.** Longitudinal cut before ((a–f) up) and after ((a–f) down) rotation correction.

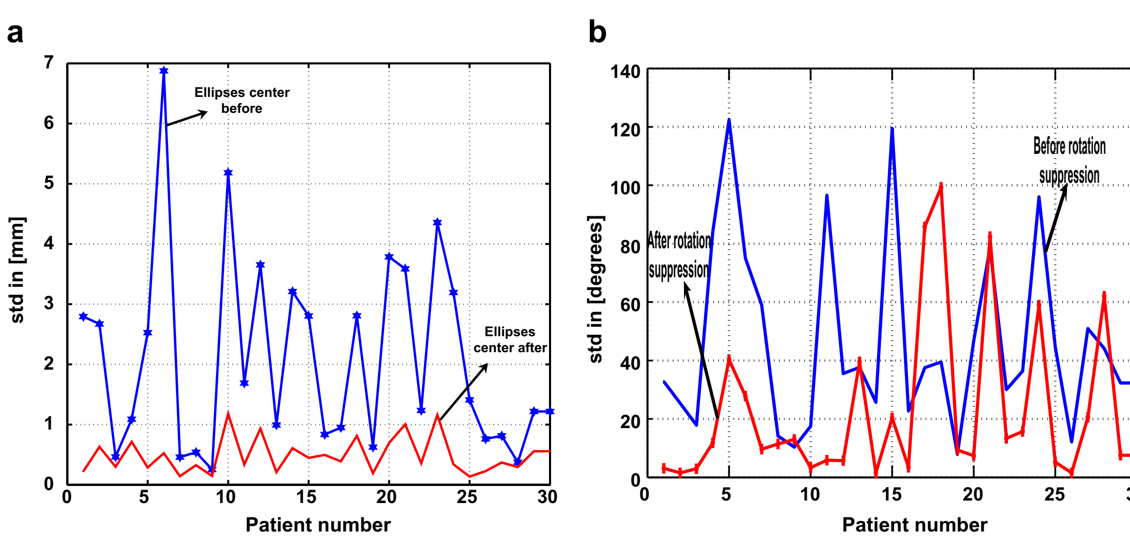


**Fig. 12.** Standard deviation of motion parameters before (blue) and after (red) rotation suppression: ellipses centers (a) and rotation angle (b).

$$x(t) = a_g(t)\cos(\theta + \delta_g(t)) + c_{xg}(t),$$
$$y(t) = b_g(t)\sin(\theta + \delta_g(t)) + c_{yg}(t), \quad z(t) = vt$$

Fig. 14a shows a static vessel reconstruction of an IVUS pullback of 1090 images corresponding to 25 mm long vessel segment. Fig. 14 shows the 2.5-D graphical representation of the segment before

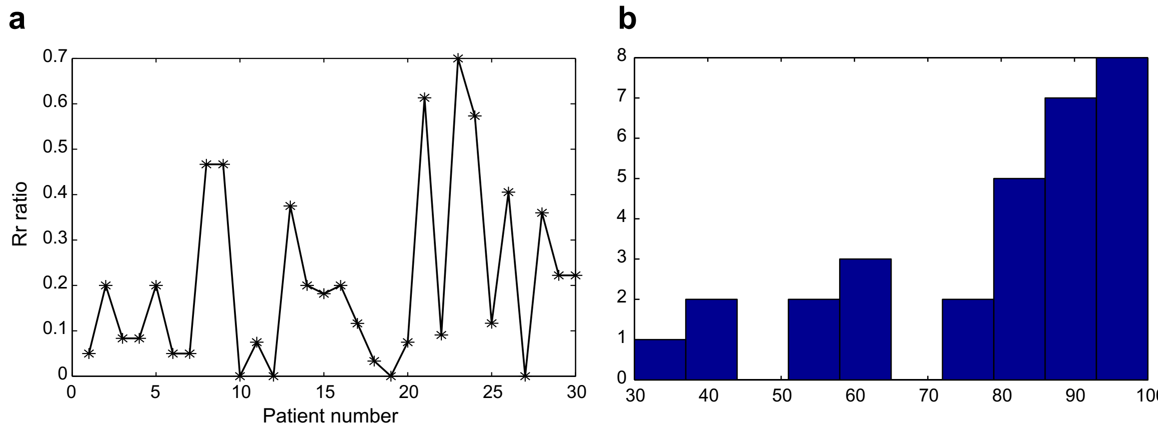


**Fig. 13.** Movement reduction in experimental data: reduction ratio for the 30 patients (a) and histogram of reduction percentage (b).

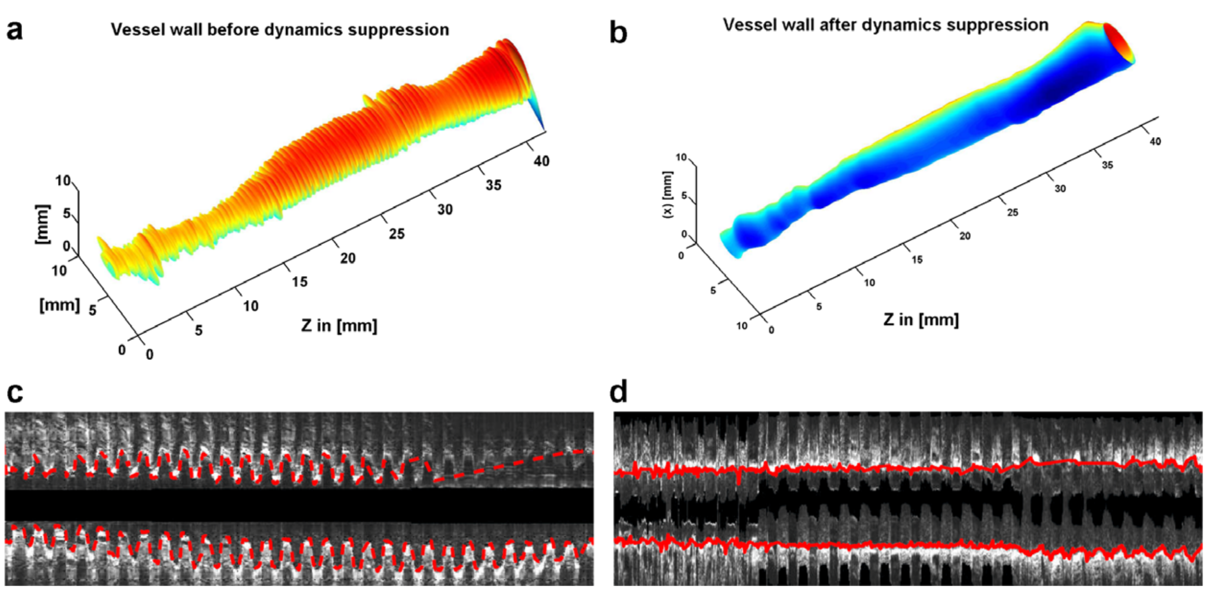


**Fig. 14.** Static vessel model: two views of 2.5-D vessel wall reconstruction before (a) and after (b) dynamic suppression and the corresponding longitudinal IVUS cuts before (c) and after (d) motion suppression.

(a) and after (b) dynamics suppression. Fig. 14c and d illustrate the corresponding longitudinal IVUS cuts before and after motion compensation.

## 5. Discussions

### *5.1. Elliptical fitting of vessel borders*

When considering the problem of image registration and alignment, a natural question is which general strategy to use: image-based (where all pixels of the images contribute to the estimate of the image transformation) or landmark-based (only some, usually having special meaning, points of the images are taken into account in order to align the images). Our approach follows the second strategy aligning the elliptic approximations to a set of points corresponding to the lumen-tissue transition. Although an ellipsoidal shape can not exactly approximate the vessel wall shape, such inaccuracies do not affect the performance of the proposed approach since its purpose is to estimate the rigid transformation of the vessel. By using an elliptical approximation of the vessel represents a global approach to detect motion and rotation of the vessel; at the same time the elliptical approximation is able to better cope with small errors in the classification of the contour points by the neural network (compared to a flexible snake model or other local deformable models).

Empirically, we found that in 88% of segmented images the elliptical shape model could approximate the vessel being the rest of images mainly cases of bifurcations to main vessels and large NURD artifacts. In order to evaluate the quality of the vessel approximation, we estimated a distance map of the found contour points by the neural network and approximated the vessel points by the elliptical model. We consider that the elliptical model approximation is correct if the value of its points on the distance map is less than a given epsilon. In our case, epsilon was set empirically to 0.2 mm. Fig. 16 shows the mean error and standard deviation of estimated distances as well as their histograms. In case the distance surpasses this threshold, a hypothesis for a segmentation failure is generated and the frame corresponding to this part of the vessel is disregarded from analysis and motion estimation is

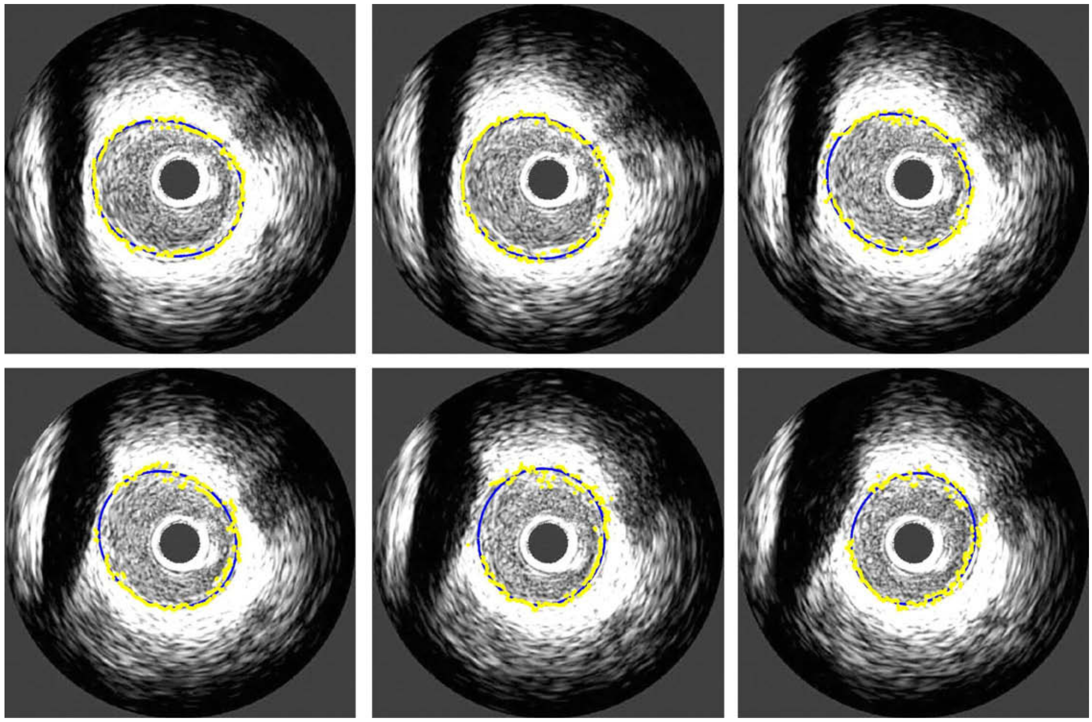

**Fig. 15.** Segmented vessel wall by neural network (in yellow) and fitted ellipse (in blue).

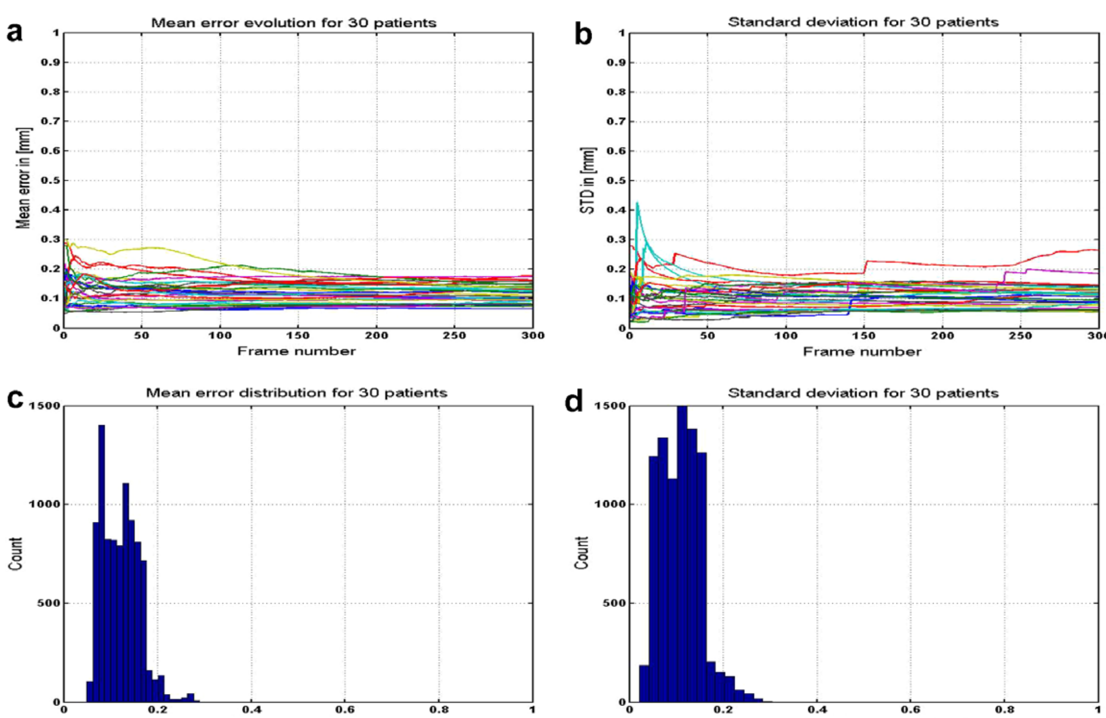


**Fig. 16.** Mean error ($\epsilon_k$) (a) its standard deviation (b) between segmented points by the neuronal network and the adjusted ellipse. The corresponding histogram are given in (c) and (d).

computed aligning the next valid frame. Finally, dynamic parameters of the failed frame are computed by interpolation of the neighbor valid frames. Elliptical fitting quality can be visually checked in the images of Fig. 15, where we show the points extracted from the neural network (in yellow) and the fitted ellipse (in blue) for six consecutive frames.

From our tests on the 30 patients IVUS videos we conclude the following:

(a) Our methodology is not affected by calcified plaque presence as it presents an abrupt transition from lumen to tissue which is easily identified by the neural network (see Fig. 17a).

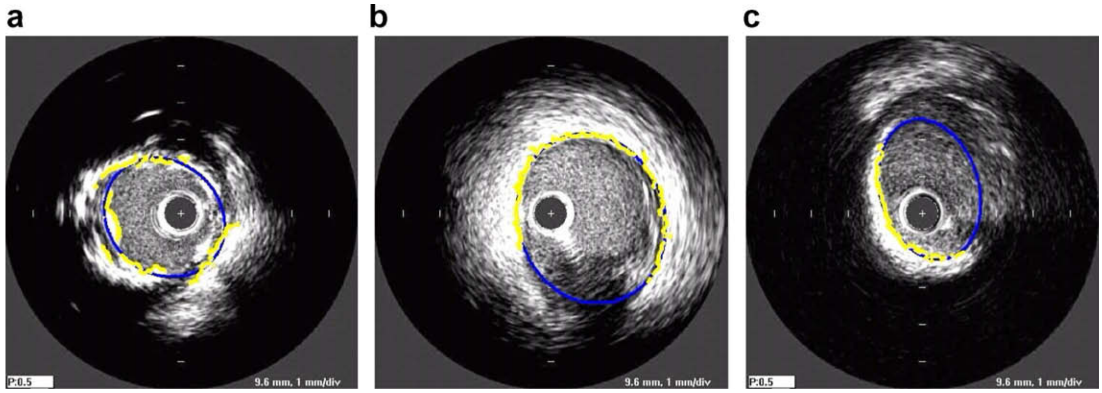


**Fig. 17.** Performance in the presence of artifacts: calcification (a), guide artifact (b) and bifurcations (c).

(b) Imaging artifacts, such as sensor guide, constitute sparse phenomena leading to local responses in the short-axes image view that do not affect the ellipse approximation (see Fig. 17b).
(c) In the case of NURDS, such sequences are of limited clinical interest by their low quality (impossibility to quantify vessel structures) and are out of the scope of our analysis, neither recommended to be quantified in clinical studies. Still, the procedure for elliptical fitting is valid provided that the NURD artifact does not affect more than 30% of the vessel.

### 5.2. Motion artifact removal

The complex motion of the imaging catheter inside the coronary vessel causes motion artifacts that can be approximated by three phenomena: (a) rotation of the IVUS imaging catheter with respect to the vessel (i.e., around the axis tangential to the catheter), (b) translation of the imaging catheter in the plane perpendicular to the catheter axes, and (c) translation of the catheter along its axis forward and backward causing a swinging effect.

In this paper, we address the first two motion artifacts in order to help the short-axis as long-axis vessel display, to visualize and quantify different morphological vascular structures like plaque, stents, lumen diameter, lesions, etc. The intrinsic rotation and translation of the imaging catheter (related to type (a) and (b)) introduce artifacts in the longitudinal views making structures to appear and disappear as well as provoking tooth-shaped adventitia and calcified plaque, etc. This motion mainly affects the computation of the vessel diameter in the L-views. In the short-axis view, the rotation and translation of the catheter lead to high amount of vessel motion.

By applying our stabilization approach, vessel appearance in short-axes views allows better and easier perception of vessel structures distribution and quantity. In longitudinal views we remove the tooth-shape and thus assure that changes in vessel diameter are due to changes in morphology. In this way, we improve the analysis of plaque progression along the vessel compared to the original L-views. Note that this step is crucial for a further analysis of vessel biomechanics (palpography, measuring elastic properties as strain or stress, etc.) since their computation requires tracking material points of the vessel along the cardiac cycle.

Reliable length measurements along the vessel must either account (i.e. correct) for catheter swinging or simulate image-based ECG-gating. We note that the cardiac components of the rotational angle can serve to simulate an ECG-gating by sampling the sequence at the right (cardiac) rate. Therefore, although we do not explicitly address it, our estimation of dynamics enables reliable volumetric measurements as well as exploring vessel (continuous) elastic properties by keeping the original information (complete set of data O'Malley et al., 2006).

### 5.3. Our approach and IVUS gating

In this paper we deal with the problem of rotation suppression of IVUS images that can be observed in non ECG-gated as well as ECG-gated sequences. Thus, our approach is not depending and completely applicable to ECG-gated procedures (based on hardware or image-gating). ECG-gating has the advantage to allow more precise longitudinal measurements; the price to be paid consists of increasing the acquisition time in up to 7 times with respect a non-gated motorized pullbacks at 0.5 mm/seg. (von Birgelen et al., 1997), which results in an increase of the intervention time of the patient. Besides the special acquisition devices are not commonly available at all medical centers. The above reasons have recently motivated the development of image-based ECG-gated IVUS (Seemantini et al., 2005; De Winter et al., 2004). Such techniques discard part of the information (frames) available in an IVUS sequence. Since in our approach to align images we do not put any constraint on the pair of images, our approach allows using the whole stack of IVUS images provided by the acquisition device as well as the ECG-gated subset of images in order to overcome the misalignment artifacts introduced by vessel rotation and translation.

Current ECG-gating as well image-gating approaches still can suffer from the image rotation artifacts making difficult to address problems as palpography estimation, plaque following along the vessel, volumetric measurements, etc. Moreover, although we do not explicitly address it, we note that the cardiac components of the rotational angle can serve to simulate an ECG-gating by sampling the sequence at the right (cardiac) rate. Therefore, our estimation of dynamics enables reliable volumetric measurements as well as exploring vessel (continuous) elastic properties by keeping the original information (complete set of dataO'Malley et al., 2006).

### 5.4. Catheter oscillating obliquity

Cardiac dynamics introduce two main artifacts affecting the catheter trajectory. Firstly, due to the change in vessel curvature during the cardiac cycle, the catheter moves along the axis of the vessel (longitudinal displacement). This forward and backward displacement implies that, in a mechanical pullback, IVUS images are not uniformly distributed along the sequence $z$-axis. Secondly, tilting of the catheter introduces an anisotropic scaling of IVUS cross sections if the catheter is not coaxial within the vessel. Such phenomenon produces a more elliptical shaped vessel, which might result in an overestimation of the area and a misinterpretation of the vessel shape (Mintz et al., 2001).

Correction of catheter longitudinal movement would require a dynamic model of the catheter 3-D trajectory and is out of the scope of the presented work. Tilting of the catheter cross-sectional plane can not be properly corrected unless a complete 3-D reconstruction and modelling of the vessel and the catheter inside the vessel are available. Since we aim at improving 3-D IVUS without affecting vessel measurements such as length or area, catheter obliquity will be disregarded.

### 5.5. Radial deformation of the coronary vessel

Radial deformation of cardiac arteries is mainly due to blood pressure and vessel wall elastic properties. By Hooke's law (Mazumdar, 1992; Nadkarni et al., 2003; Holzapfel and Weizsäcker, 1998; Humphrey, 1995), the radial increment, $\nabla r$, is proportional to the gradient of blood pressure, $\nabla P$ via the relation (Mazumdar, 1992; Nadkarni et al., 2003; Holzapfel and Weizsäcker, 1998; Humphrey, 1995):

$$\nabla r = (\kappa \Delta P/\pi)^{1/2} \tag{11}$$

where $\kappa$ is the elasticity coefficient. At vessel sections presenting non homogenous plaque, the elasticity coefficient varies for each pixel. In order to estimate the radial deformation, it suffices to use a constant elastic coefficient (Hook's law for uniform media) describing the average deformation ranges of the vessel wall.

According to clinical studies (Williams et al., 1999), $\kappa$ is in the range $\kappa = (0.010 \pm 0.020)\,\text{mm}^2/\text{mmHg}$ and $\Delta P \approx 40\,\text{mmHg}$. By Hook's law (11), it follows that $\nabla r \approx 0.35$ mm. Taking into account that the radii of coronary segments (Dodge et al., 1992) is in the range $r = 2.64 \pm 0.3$ mm, we have that the relative radial deformation induced by blood pressure scaling is $\delta r = (\nabla r/r) \times 100 \approx 13\%$.

Applying scaling of the vessel in the IVUS images might remove the deformation due to the blood pumping that is directly related to the elasticity of the vessel. Besides the existing radial scaling does not affect the computation of the translation and rotation parameters. Therefore, radial scaling is not included into the model formulation.

### 5.6. Clinical applicability

The methodology proposed and its implementation improve the visualization in short-view IVUS videos as well as in the longitudinal views with a success of correctly aligned sequences. Currently, the methodology is to be implemented in a package for IVUS analysis and plaque characterization to be installed in clinical conditions.

On the other hand, the proposed methodology for rotation suppression has different possible clinical applications:

1. *General measures extraction from stabilized IVUS sequence*. We consider that this application is a first and necessary step towards: (a) Estimation of geometric parameters such as vessel length using longitudinal cuts views based on methodology applying the ECG-gating to address the swinging artifacts of the IVUS catheter. (b) Vessel wall strain estimation by palpography. In order to obtain valid strain estimation, we consider that palpography extraction needs: first, alignment of images and second, determining the frames corresponding to end-systole and end-diastole peaks (being estimated by ECG-signal or image analysis).
2. *Heart dynamic estimation*. Being possible to separate the geometric contribution from dynamics contribution, we developed the basis to 2.5-D vessel reconstruction only using IVUS data. This method can give promising evidences for vessel wall dynamics estimation such as the introduction of an alternative technique to estimate local heart dynamics. In this way, we provide a new possibility of studying the vessel dynamics and geometry as well as establishing new diagnostic tools. For example, an extensive study of IVUS rotation profile versus pumping heart efficiency obtained experimentally using diastolic and systolic angiography heart views, can hint a positive correlation between heart rotation and pumping heart efficiency.

## 6. Conclusions

In this article we developed a geometric and kinematic model in order to study the evolution of coronary artery wall. The model is based on the assumption that the evolution of the arterial wall can be modeled assuming two principal contributions that come from different physical reasons. The first one, a systematic contribution caused by geometric intrinsic arterial properties, and the second one, an oscillating contribution that comes from ventricle dynamics. These contributions govern in major degree the profiles appearance of arterial wall in longitudinal views. Using this assumption, we propose a methodological strategy in order to estimate and suppress rigid IVUS dynamical distortions.

IVUS image alignment is very important in problems that study vessel deformation along the cardiac cycle, such as palpography which compares deformations at diastole and systole. Exploring vessel wall kinematics needs vessel border points tracking in order to extract vessel deformation and to judge about coronary elasticity. Definitely, image rotation observed in current IVUS sequences hinders the tracking of the corresponding points/zones of the vessel border. On the other hand, the accurate radial deformation of the vessel on the image not only depends on the mutual image/vessel rotation, but also on the artifact produced by the oscillating longitudinal obliquity that is induced by the ventricle pulsatile dynamics. Usually, oscillating longitudinal catheter motion is overcome by ECG-gated or image-gated sequence construction that improves significantly the longitudinal view of the vessel, but acquires a picture of the vessel shape only in diastole (De Winter et al., 2004). Looking for alternative technical approaches to solve the problem of image spatial location covering the whole cardiac cycle is another research opportunity to advance in the more accurate longitudinal visualization, vessel radial deformation analysis, vessel/plaque elasticity estimate, prediction of atherosclerotic accumulation and possible plaque ruptures from IVUS data.

Separating the geometric contribution from dynamical contribution can be the fundamental basis to 2.5-D vessel reconstruction only using IVUS data and could be an important advance in vessel wall dynamics estimation that introduces an alternative technique to estimate local heart dynamics. In this way, we provide a new possibility of studying robustly the vessel dynamics, creating statistical models of vessel dynamics and establishing new diagnostic tools.

## Acknowledgement

We would like to thank Carlos Rodríguez from the Mathematical Dep. of the Universitat Autonoma de Barcelona for his support and advise. This work was supported in part by a research grant from projects TIN2006-15308-C02, FIS-PI061290, PI070454 and PI071188 and CONSOLIDER-INGENIO 2010 (CSD2007-00018). The last author has been supported by The Ramón y Cajal Program.

## References

Andrew, F., Maurizio, P., Robert, B., 1999. Direct least square fitting of ellipses. IEEE Trans. Pattern Anal. Mach. Intell. 21 (5), 476–480.

Berry, E., Kelly, S., Hutton, J., Lindsay, H., et al., 2000. Intravascular ultrasound-guided interventions in coronary artery disease, NHS RD HTA Programme.

Boston Scientific Corporation, 1998. Scimed division, The ABCs of IVUS.
Broucke, R., 1978. Lagrangian and Hamiltonian methods in the theory of rotational motion of a rigid body. IASOM TR-78-7. The University of Texas at Austin.
Bruining, N., von Birgelen, C., Feyter, P., et al., 1998. ECG-gated versus nongated three-dimensional intracoronary ultrasound analysis: implications for volumetric measurements. Cathet. Cardiovasc. Diagn. 43 (3), 254–260. Thoraxcenter, Department of Cardiology, Erasmus Medical Center and Erasmus University, Rotterdam, The Netherlands.
Courtney, B., Robertson, A., Maehara, A., et al., 2002. Effects of transducer position on backscattered intensity in coronary arteries. Ultrasound Med. Biol. 28 (1), 81–91.
Danilouchkine, M., Mastik, F., van der Steen, A., 2006. Scale space optical flow with feature-based weighting scheme for quantitative assessment of rotational tissue motion in IVUS. In: International Workshop on Computer Vision for Intravascular and Intracardiac Imaging in MICCAI, Copenhaguen, Denmark.
de Korte, C., 1999. Intravascular Ultrasound Elastography. Interuniversity Cardiology Institute of the Netherlands (ICIN).
Delachartre, P., Cachard, C., Finet, G., Gerfault, F., Vray, D., 1999. Modeling geometric artefacts in intravascular ultrasound imaging. Ultrasound Med. Biol. 25 (4), 567–575.
De Winter, S., Hamers, R., Degertekin, M., et al., 2004. Retrospective image-based gating of intracoronary ultrasound images for improved quantitative analysis: the intelligate method. Catheter Cardiovasc. Interv. 61 (1), 84–94. Thoraxcentre, Department of Cardiology, Erasmus MC, Rotterdam, The Netherlands.
De Winter, S., Hamers, R., Degertekin, M., Tanabe, K., Lemos, P., Serruys, P., Roelandt, J., Bruining, N., 2004. Retrospective image-based gating of intracoronary ultrasound images for improved quantitative analysis: the intelligate method. Catheter Cardiovasc. Interv. 61, 84–94.
Dijkstra, J., Wahle, A., Koning, G., Reiber, J., Sonka, M., 1998. Quantitative coronary ultrasound: state of the art. What's New Cardiovascular Imaging, 79–94.
Di Mario, C., Madretsma, S., Linker, D., et al., 1993. The angle of incidence of the ultrasonic beam a critical factor for the image quality in intravascular ultrasonography. Am. Heart J. 125, 442–448.
Mario, Di, von Birgelen, C., Prati, F., et al., 1995. Three-dimensional reconstruction of cross sectional intracoronary ultrasound: clinical or research tool. Br. Heart. J. 73 (5), 26–32 (Suppl. 2).
Dodge, J., Brown, B., Bolson, E., Dodge, H., 1992. Lumen diameter of normal human coronary arteries. Influence of age, sex, anatomic variation, and left ventricular hypertrophy or dilation, Department of Medicine, University of Washington, Seattle, Circulation. 86(1), 232–246.
Evans, J., Ng, K., Wiet, S., et al., 1996. Accurate three-dimensional reconstruction of intravascular ultrasound data: spatially correct three-dimensional reconstructions. Circulation 93 (3), 567–576.
Giannattasio, C., Failla, M., Emanuelli, G., et al., 2001. Local effects of atherosclerotic plaque on arterial distensibility. Hypertension 38 (5), 1177–1180.
Gil, R., von Birgelen, C., Prati, F., Di Mario, C., Ligthart, J., Serruys, P., 1996. Usefulness of three-dimensional reconstruction for interpretation and quantitative analysis of intracoronary ultrasound during stent deployment. Am. J. Cardiol. 77, 761–764.
Graham, S., Brands, D., Sheehan, H., et al., 1989. Assessment of arterial wall morphology using intravascular ultrasound in vitro and in patient. Circulations II-56.
Holzapfel, G., Weizsäcker, H., 1998. Biomechanical behavior of the arterial wall and its numerical characterization. Comp. Biol. Med. 28, 377–392.
Holzapfel, G., Gasser, T., Stadler, M., 2002. A structural model for the viscoelastic behavior of arterial walls: continuum formulation and finite element analysis. Eur. J. Mech. A-Solids 21, 441–463.
Humphrey, J., 1995. Mechanics of arterial wall: review and directions. Critical Rev. Biomech. Eng. 23, 1–162.
Jensen, J., 2001. Linear description of ultrasound imaging system. Notes for the International Summer School on Advanced Ultrasound Imaging, Technical University of Denmark.
Jumbo, G., Raimund, E., 1998. Novel techniques of coronary artery imaging. In: Beyond Angiography, Intra Vascular Ultrasound, State of the Art, vol. XX. Congress of the ESC Vienna-Austria, University of Essen, Germany.
Kittel, C., Knight, W., Ruderman, M., 1991. Mechanics, Berkeley Physics Course, vol. 1, Reverté.
Lester, H., Arridge, S., 1999. A survey of hierarchical non-linear medical image registration. Pattern Recogn. 32, 129–149.
Leung, K., Baldewsing, R., Mastik, F., Schaar, J., Gisolf, A., van der Steen, A., 2005. Motion compensation for intravascular ultrasound palpography for in vivo vulnerable plaque detection. IEEE Ultrason. Symp., pp. 253–256.
Leung, K., Baldewsing, R., Mastik, F., Schaar, J., Gisolf, D., 2006. Motion compensation for intravascular ultrasound palpography. IEEE UFFFC 53, 1269–1280.
Mazumdar, J., 1992. Biofluids Mechanics. World Scientific Publishing.
Metz, J., Paul, G., et al., 1992. In: Tobis, Jonathan M., Yock, Paul G. (Eds.), Intravascular Ultrasound Imaging. Churchil Livinstone Inc.
Metz, J., Paul, G., Fitzgerald, P., 1998. Intravascular ultrasound basic interpretation. In: Beyond Angiography, Intravascular Ultrasound, State of the art, vol. XX, Congress of the ESC Vienna-Austria, California, USA.
Mintz, G., Nissen, et al., 2001. ACC Clinical Expert Consensus Document on IVUS JACC 37, 1478–1492.
Mintz, G., Nissen, S., et al., 2001. Clinical expert consensus document on standards for acquisition, measurement and reporting of intravascular ultrasound studies (IVUS). J. Am. Coll. Card. 37 (5), 1478–1492.
Nadkarni, S., Austin, H., et al., 2003. A pulsating coronary vessel phantom for two- and three-dimensional intravascular ultrasound studies. Ultrasound Med. Biol. 29 (4), 621–628.
Nadkarni, S., Boughner, D., Aaron, F., 2005. Image-based cardiac gating for three-dimensional intravascular ultrasound. Ultrasound Med. Biol. 31 (1), 53–63.
Nissen, S., 2002. Application of intravascular ultrasound to characterize coronary artery disease and assess the progression or regression of atherosclerosis. Am. J. Cardiol. 89 (Suppl.), 24B–31B.
Nissen, S., Yock, P., 2001. Intravascular ultrasound: novel pathophysiological insights and current clinical applications. Circulation 103 (4), 604–616.
O'Malley, Sean M., Naghavi, Morteza, Kakadiaris, Ioannis A., 2006. Image-based frame gating for contrast-enhanced IVUS sequences. In: International Workshop on Computer Vision for Intravascular and Intracardiac Imaging in MICCAI, Copenhaguen, Denmark.
O'Malley, S., Carlier, S., Naghavi, M., Kakadiaris, I., 2007. Image-based Frame Gating of IVUS Pullbacks: a Surrogate for ECG. ICASS'2007, Hawaii, USA (April).
O'Malley, S., Granada, J., Carlier, S., Naghavi, M., Kakadiaris, I., 2008. Image-based gating of intravascular ultrasound pullback sequences. IEEE Trans. Inform. Technol. Biomed. 12 (3), 299–306.
Patrick, H., 1994. Intelligencia Artificial. Addison Wesley Iberoamericana.
Pluim, J., Maintz, A., Viergever, M., 2003. Mutual Information based registration of medical imaging: a survey. IEEE. Med. Imag. 20.
Roelandt, J., Di Mario, C., Pandian, N., et al., 1994. Three-dimensional reconstruction of intracoronary ultrasound images. Rationale, approaches, problems, and directions. Circulation 90 (2), 1044–1055.
Rosales, M., Radeva, P., et al., 2004. Simulation Model of Intravascular Ultrasound Images, Lecture Notes in Computer Science Publisher: Springer-Verlag Heidelberg, Medical Image Computing and Computer-Assisted Intervention MICCAI 2004, France, vol. 3217/2004, pp. 200–207 (September).
Rosales, M., Radeva, P., Rodríguez, O., Gil, D., 2005. The IVUS image rotation effect: Part I (The effect subtraction). In: FHIM Proceedings. LNCS, Vol. 3504. Springer-Verlag, pp. 359–368.
Seemantini, Nadkarni, K., et al., 2005. Image-based cardiac gating for three-dimensional intravascular ultrasound. Ultrasound Med. Biol. 31 (1), 53–63.
Thrush, A., Bonnett, D., Elliott, M., Kutob, S., Evans, D., 1997. An evaluation of the potential and limitations of three-dimensional reconstructions from intravascular ultrasound images. Ultrasound. Med. Biol. 23 (3), 437–445.
Vogt, M., et al., 1998. Structural analysis of the skin using high frequency broadband ultrasound in the range from 30 to 140 MHz, IEEE Int. Ultrason. Symp., Sendai, Japan.
von Birgelen, C., de Vrey, E., Mintz, G., Nicosia, A., Bruining, N., Li, W., Slager, C., Roelandt, J., Serruys, P., de Feyter, P., 1997. ECG-gated three-dimensional intravascular ultrasound: feasibility and reproducibility of the automated analysis of coronary lumen and atherosclerotic plaque dimensions in humans. Circulation 96, 2944–2952.
Wahle, A., Prause, P., DeJong, S., Sonka, M., 1999. Geometrically correct 3-D reconstruction of intravascular ultrasound images by fusion with biplane angiography. Methods and validation. IEEE Trans. Med. Imaging 18 (8), 686–699.
Waks, E., Prince, J., Andrew, S., 1996. Cardiac motion simulator for tagged MRI. In: Proceeding of MMBIA. IEEE. John Hopkins University, Baltimore.
Williams, M., Stewart, R., Low, C., et al., 1999. Assessment of the mechanical properties of coronary arteries using intravascular ultrasound: an in vivo study. Int. J. Card Imag. 15 (4), 287–294.
Yock, P., Linker, D., Saether, O., et al., 1988. Intravascular two-dimensional catheter ultrasound, Initial clinical studies. Circulations II-21 (78).
Young, B., Heath, J., 2000. Wheater's, Histología Funcional, 4ta edición, Ediciones Hardcourt, S.A.